# Quantifying damage in polycrystalline ice via X-Ray computed micro-tomography

Authors: Kevin Hammonds and Ian Baker



Hammonds, Kevin, and Ian Baker. "Quantifying damage in polycrystalline ice via X-Ray computed micro-tomography." Acta Materialia 127 (April 2017): 463-470. DOI: 10.1016/j.actamat.2017.01.046.

# Quantifying damage in polycrystalline ice via X-Ray computed micro-tomography

Kevin Hammonds [a], [b], [*], Ian Baker [a]

[a] Thayer School of Engineering at Dartmouth College, Hanover, NH, USA
[b] Montana State University, Department of Civil Engineering, Bozeman, MT, USA

A B S T R A C T

The use of X-ray computed micro-tomography (micro-CT) is presented here as a useful tool for the analysis and quantification of damage in polycrystalline ice. Although known to be useful for characterizing damage in many other materials, the use of micro-CT has not yet been adapted to the non-trivial case of also characterizing damage in polycrystalline ice. Samples of polycrystalline ice were tested in uniaxial compression at six different strain rates, spanning four orders of magnitude, from $1 \times 10^{-6}$ s$^{-1}$ to $1 \times 10^{-3}$ s$^{-1}$, and two different testing temperatures of $-10$ °C and $-20$ °C. The extent of cracking from each test is characterized via micro-CT imaging and is quantified via a newly proposed variant of the crack density tensor, which accounts for any anisotropy in the mean crack orientation and is shown to be equivalent to the materials anisotropy tensor. To account for anisotropy in the distribution of cracks, an eigenanalysis is also performed. The results show that micro-CT can be a useful tool for both visualizing and quantifying damage in polycrystalline ice and that a 3-D analog of the traditional second-rank crack density tensor can be readily calculated via commercially available software.

## 1. Introduction

Over the last two decades, the use of X-ray computed micro-tomography (micro-CT) has become a widely used laboratory technique for many applications in materials science and engineering [1,2]. Underlying much of this broad appeal is the ability of micro-CT to nondestructively characterize material microstructures at a micron resolution in three dimensions. To date, micro-CT has been successfully employed to characterize an extensive variety of materials and processes, such as bone porosity [3], brine channels and air inclusions in sea ice [4], the fracture and damage of concrete [5], the microstructural evolution of snow under a temperature gradient [6], fatigue crack propagation in cast-iron [7], etc. Although not nearly an exhaustive list, one area of study where the advantages of micro-CT have not yet been fully realized, is the study and 3-D characterization of damage in strained polycrystalline ice. Developing such an understanding is thought to be of critical importance to better predicting the fracture mechanics of both land-based and sea-based ice flows and is thus the primary focus of this work.

Like many other materials, ice can sustain damage in the form of non-propagating cracks that result from localized strains [8]. The presence of these cracks, in turn, can have dramatic affects on the material properties of the ice, even though the larger body remains fully intact. Understanding the role of deformation and damage in polycrystalline ice, including columnar ice, has been the topic of many laboratory, field, and theoretical studies spanning the past five decades [9–16]. This interest is derived from the broad application of such knowledge, including calving rates of glaciers and ice sheets [17,18], predicting sea ice behavior in the Arctic and Antarctic oceans [19–22], structural engineering of off-shore structures in the polar regions [23–25], and interpretation of the surface characteristics of icy terrestrial bodies [26–28].

In order to quantify and validate the predictions of traditional fracture mechanics, as it would apply to ice $I_h$, there is often an imaging component of the analysis required for either the investigation of field-collected samples or laboratory tested specimens. This imaging component requires that the actual cracks be imaged such that they can be manually counted, measured, and characterized. This is an important component of the analysis, as the size, type, and number of cracks can act as benchmarks detailing the mechanical history of the ice. For example, the observation of "comb-cracks" versus "wing-cracks" along a fault may be indicative of the destabilization mechanism of the body [15], whereas evidence of intergranular versus transgranular fracture may be more telling about the response of the ice to either elastic or plastic deformation [29], respectively.

Similar to many polycrystalline metals and alloys, the study of polycrystalline ice via micro-CT has previously been thought of as a poor choice of materials for micro-CT analysis, as no other microstructural information can be elucidated and x-ray attenuation in ice can be quite high [4]. Given sufficient voiding, cracking, or pore space is present within the material, however, the use of polychromatic x-ray sources has been shown to be useful, predominantly only limited by camera resolution. This has been evidenced by other recent micro-CT studies pertaining to sea ice inclusions [4], the bonding of ice spheres [30], and the metamorphism of ice-snow interfaces [31].

## 2. Background

### 2.1. Crack density tensor

A very recent and detailed review of the various ways to measure and quantify damage in polycrystalline ice is given in Snyder et al. (2015) [8] and is not repeated here. To summarize, however, most approaches involve first the concession of a 3-D perspective to a 2-D perspective, such that all cracks within a 2-D plane can be differentiated and then manually measured and counted. Making such measurements is quite tedious work, as both the crack length and the normal orientation of the crack from a fixed point of reference is required. With this information, a dimensionless 2-D crack density tensor $\alpha_{2-D}$ can be derived

$$\alpha_{2-D} = \frac{1}{A}\sum_i \left(c^2 \vec{n}\,\vec{n}\right)_i \tag{1}$$

where $A$ is the cross-sectional area of the sample, $c$ is the crack half-length, and $\vec{n}$ is the unit vector normal to the $i$ th crack of length $2c$ [8,32]. The vector product $\vec{n}\,\vec{n}$ denotes the dyadic, which when summed over all cracks and all orientations, gives a measure of the anisotropy of the measured crack orientation in a tensorial format as a second-rank tensor [8]. If extending to the 3-D case, Eq. (1) simply becomes

$$\alpha_{3-D} = \frac{1}{V}\sum_i \left(a^3 \vec{n}\,\vec{n}\right)_i \tag{2}$$

where $V$ is the sample volume and $a$ is the radius of the $i$ th circular-shaped crack [8,33]. In either format, the benefit of the tensorial representation is that it lends a continuum approach to understanding the damage mechanics of the material [34]. In the case of an isotropic or random distribution of crack orientations, Eqs. (1) and (2) simplify to the scalar (first invariant of the tensor), which is the trace of alpha $(tr(\alpha) = \rho_c)$.

### 2.2. Stereological analysis

Of the many variables that can be calculated with the Bruker CT analysis (CTan) software, that accompanied the Bruker Skyscan 1172 micro-CT that was used in this study, the 3-D stereological analysis is focused on here as perhaps the most beneficial in handling anisotropy and crack density distributions. Originally developed for the analysis of pore space in bone, the stereological analysis makes use of a statistical technique in which a mean intercept length is calculated in three dimensions from within a spherical volume encompassing the user-defined volume of interest (VOI) of the sample. Within this encompassing sphere, lines can be drawn in up to 1,024 different orientations with a spacing that is user-defined, but can be as small as one pixel or "voxel" (a 3-D pixel) apart. Once drawn, the orientation of each line is recorded and the length of each line is divided by the number of times it intercepts an object (voxels equal to 1 on a binary scale), this quotient defines the mean intercept length $l$. Of importance to note, is that whether or not the line drawn traverses a lone 1 pixel or ten 1 pixels, as long as these pixels are connected, this would only count as one intercept. Thus, phenomenologically, the mean intercept length could also be thought of as a metric for the length between cracks and not necessarily the crack length itself.

For the mean intercept length analysis presented in this study, the number of randomly selected orientations was set to 512 with a 90 $\mu$m (5 pixel) spacing. For perspective, this allowed for 53,625 lines to be drawn per orientation within a VOI of 4213 mm$^3$. Once complete, the number and length of all intercepts over all orientations are related back to the principal axes of the encompassing sphere, such that the three principal mean intercept lengths, $l_1$, $l_2$, and $l_3$ and unit vector orientations, $\vec{e}_1$, $\vec{e}_2$, and $\vec{e}_3$ can be determined. These orientations are solved for via the statistical fitting of an ellipsoid encompassing all mean intercept length values, when each mean intercept length is plotted as a radius anchored at the origin. Originally given in Harrigan and Mann (1984) [36], this process creates the surface of an ellipsoid of the general form

$$Ax_1^2 + Bx_2^2 + Cx_3^2 + 2Dx_1x_2 + 2Ex_1x_3 + 2Fx_2x_3 = 1 \tag{3}$$

where $A$, $B$, $C$, $D$, $E$, and $F$ are dimensionless coefficients and $x_1$, $x_2$, and $x_3$ are the principal axes of the original Cartesian coordinate system of the user-defined VOI. $\vec{e}_1$, $\vec{e}_2$, and $\vec{e}_3$ can then be solved for via an eigenanalysis, determining the rotation of the orthogonal principal axes of the ellipsoid from the original axes of the VOI, such that $\vec{e}_1$, $\vec{e}_2$, and $\vec{e}_3$ are the eigenvectors representing the orientations of $l_1$, $l_2$, and $l_3$, relative to the original Cartesian coordinate system of the VOI. Additionally, the eigenvalues $E_1$, $E_2$, and $E_3$, are calculated via an eigenanalysis, which can then be used to define the degree of anisotropy $DA$ of the VOI, where $DA = 1 - \left(\frac{E_{min}}{E_{max}}\right)$. It was also cleverly pointed out in Harrigan and Mann (1984) [35] that the coefficients of Eq. (3) can equally be given as a dimensionless tensor, which they present as the materials anisotropy tensor $M$, where $M = \begin{bmatrix} A & D & E \\ D & B & F \\ E & F & C \end{bmatrix}$. Given that $M$ is indiscriminate towards the material to which it is being applied, it is proposed in this study that it could also be used as an analog to the tensorial component of Eq. (2). Further demonstrating the many advantages of micro-CT and the commercially available software for micro-CT analysis (CTan), it should be noted that all the variables described above (i.e. $l_1$, $l_2$, $l_3$, $\vec{e}_1$, $\vec{e}_2$, $\vec{e}_3$, $E_1$, $E_2$, $E_3$, $DA$, and $M$) can be calculated and given as outputs as part of a 3-D stereological analysis.

To more plainly demonstrate and test the applicability of the CTan 3-D stereological analysis for application to problems concerning crack orientation and crack distribution in solids, two binary test-cases were created and are presented here in Fig. 1. The first, a stack of binary images alternating in layers of pixel values set to either 0 or 1, and oriented such that the 1 layers were perpendicular to the $x_3$ axis is shown in the upper panel of Fig. 1. The second example, shown in the lower panel of Fig. 1, is the same as that shown in the upper panel but rotated 90°, such that the layers with pixel values equal to 1 are parallel to the $x_3$ axis. These binary

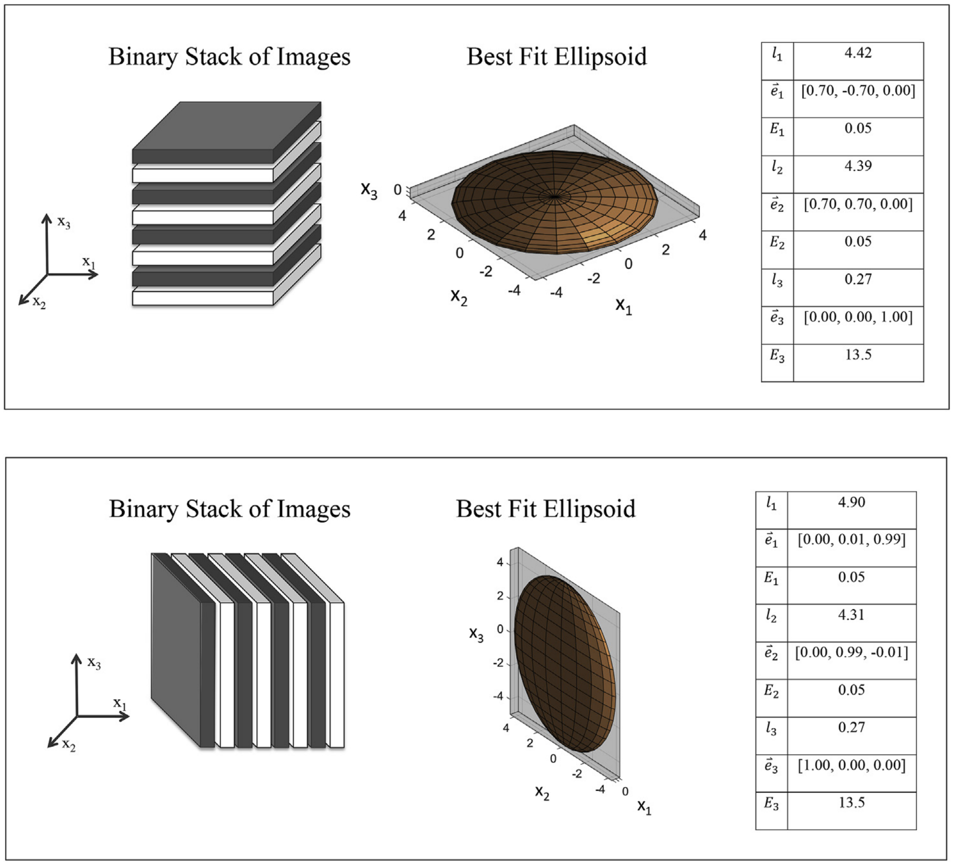


**Fig. 1.** Example from two trivial test cases (upper and lower panels) where two orthogonal stacks of alternating binary images (left) were used to illustrate the results of a 3-D stereological analysis by plotting the best fitting ellipsoid (middle) and the corresponding anisotropy via an eigenanalysis (right).

matrices are 100 × 100 × 100 pixels in size, with each pixel equaling 100 $\mu$m in resolution, thus creating a 1 cm cube that respresents alternating layers of void space (pixel values equal to 1) with a known anisotropy in layer orientation. Serving as an example set of images or "scans", the two image stacks are analyzed with the 3-D stereological analysis in CTan, as discussed above.

As would be expected, it was found that the eigenvectors with the minimum mean intercept length were perpendicular to the layering of the matrix, while the other two mean intercept lengths were much larger and nearly identical. Also shown in the upper and lower panels of Fig. 1, are illustrations of the best fitting ellipsoid about the mean intercept lengths, which clearly represent the alternating layers of 0 and 1 valued pixels and the corresponding anisotropy. Calculated values for the mean intercept length, eigenvectors, and eigenvalues are also given. The results from these two trivial cases plainly demonstrate both the convenience and potential for better quantifying damage in ice via micro-CT.

## 3. Experimental methods

### 3.1. Ice preparation

Following Cole (1979) [36], right-cylindrical specimens of pure polycrystalline ice (using Milli-Q 18.2 MΩ cm$^{-1}$ deionized water) are created via a radial freezing technique, where 0.8 mm seed grains are loaded into an aluminum mold, flooded with chilled and deaerated water, and then slowly frozen radially from the outside-inwards via a temperature controlled glycol wrap placed around the exterior of the mold. Following this approach, polycrystalline specimens of ice with a final mean grain diameter of 1 mm and a cylindrical aspect ratio of 3:1 are created (3.8 cm in diameter by 11.4 cm in length). An example of the initial polycrystalline microstructure is shown in Fig. 2, as photographed between crossed polarizing filters. An initial microstructure of randomly oriented grains ranging from 0.8 to 1.2 mm in diameter was obtained, as ascertained with polarized light microscopy and a manual calculation of the mean intercept length [37]. Following Cole (1979) [36], this initial microstructure was found to be

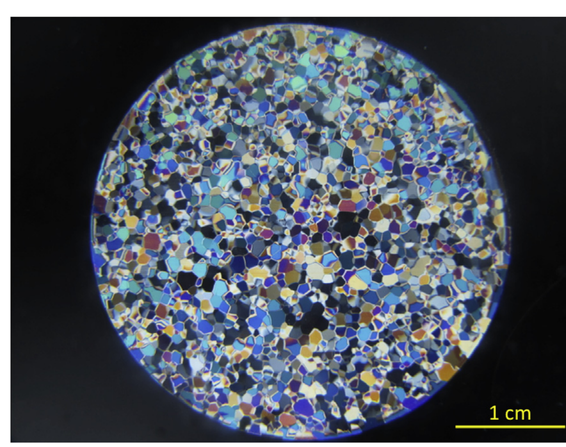


**Fig. 2.** Initial microstructure of a cylindrical specimen prepared for mechanical testing as viewed through crossed polarizing filters. Mean grain diameters were typically on the order of 1 mm. Adapted from Hammonds & Baker 2016.

reproducible.

### 3.2. Mechanical testing

Uniaxial compression tests are carried out using a MTS servo-hydraulic testing apparatus housed in a cold room. At a test temperature of $-10$ °C ( ±0.2 °C), six constant strain rates of $1 \times 10^{-3}$ $s^{-1}$, $1 \times 10^{-4}$ $s^{-1}$, $1 \times 10^{-5}$ $s^{-1}$, $5 \times 10^{-6}$ $s^{-1}$, $2.5 \times 10^{-6}$ $s^{-1}$, and $1 \times 10^{-6}$ $s^{-1}$ were applied. At a test temperature of $-20$ °C ( ±0.2 °C), two constant strain rates of $1 \times 10^{-5}$ $s^{-1}$ and $1 \times 10^{-6}$ $s^{-1}$ were applied. All compression tests were terminated at an engineering strain of 5%, which was always after the peak stress had been obtained. Here, it should be noted that, apart from the samples tested at $1 \times 10^{-3}$ $s^{-1}$, these are the same samples as those used for the mechanical testing data shown in Hammonds & Baker (2016) [38] for undoped polycrystalline ice, thus the stress-strain results from these mechanical tests are not repeated here.

At the completion of each mechanical test, two cross-sectional volumes of ice were cut with a precision bandsaw for damage analysis via micro-CT. These two test-volumes were at least 2 cm in height and 3.8 cm in diameter. This was done for two of the four test specimens used per each applied strain rate and temperature, resulting in a total of 32 cross-sectional test-volumes that were scanned and analyzed via micro-CT. Between the periods of mechanical testing and micro-CT analysis, all specimens were stored at $-30$ °C ( ±0.2 °C) to prevent any significant microstructural change in the ice.

### 3.3. X-ray computed micro-tomography (micro-CT)

For the micro-CT imaging of cracks, a Bruker Skyscan 1172 desktop micro-CT housed in a $-10$ °C cold room was used. For all samples, the X-ray beam was set to 40 kV and 250 mA. The sample was placed on the scanning stage such that the long cylindrical axis (z-axis or $x_3$) was oriented perpendicular to the X-ray beam. The sample was then rotated 180° in the x-y plane (or $x_1$-$x_2$ plane) at 0.7° increments while being scanned. Attenuation profiles were captured using a 1.3 Mp, 12-bit, cooled CCD Hamamatsu camera. Using a 15 µm resolution, the actual scanned volume of the sample was 1.9 cm in diameter by 1.5 cm tall (the VOI). If using the supplied software to perform multiple scans in one session, it would be possible to scan the entire sample, but that was not done here as the VOI from one individual scan was thought to be large enough to capture a representative volume of cracks and orientations.

Image post-processing and three dimensional image reconstruction were performed using Bruker NRecon software, which included thermal drift correction, post alignment, removal of ring artifacts, Gaussian pixel smoothing, and a beam hardening correction. Because the resulting images from the reconstruction are on a 0–255 grayscale, they must then be converted to binary images, such that they can be analyzed as individual pixels made up of either 0's (ice) or 1's (air/crack) on a binary scale. To allow for absolute control of the binary conversion, grayscale images were converted using Matlab's image processing toolbox, although CTan could have also been used. As per visual inspection, this yielded satisfactory results overall, but it should be noted that the threshold chosen for the conversion will ultimately create noise in some images while potentially deleting parts of the "objects of interest" in others. Therefore, for each sample scanned, a representative set of images must be visually inspected upon conversion to assure that the objects of interest (cracks) are being accounted for while the noise from the binarization is kept to a minimum. To illustrate this point, a typical binary conversion is shown in Fig. 3, where two different thresholds were chosen for the same 2-D grayscale image taken from a sample tested at $-10$ °C and $1 \times 10^{-3}$ $s^{-1}$ (Fig. 3a). Notice that neither images Fig. 3b or c perfectly capture the full and unbiased extent of the micro-cracks observed in the grayscale image, but Fig. 3b yields more accurate results than Fig. 3c. When performing a 2-D or 3-D quantitative analysis based on the number and location of binary pixels (0 or 1), an appropriate threshold must always be first manually chosen and then applied to the entire stack of images.

## 4. Results

### 4.1. Damage

The most easily obtainable metric for imparted damage $D$ from a binary micro-CT reconstruction is a simple cavity volume fraction of air to ice (i.e. $D = V_{air}/V_{ice}$) from within a given VOI. This approach can be useful if considering the evolution of damage within a material over periods of varying stress, strain, or time [8,39]. Expressed as a percentage, $D$ is shown in Fig. 4 as the mean value for all scans performed of all samples over a given strain rate. In this figure, $D$ monotonically increases upon increasing the applied strain rate at $-10$ °C and $-20$ °C, as would be expected. What is missing from this analysis, however, is additional information pertaining to the number of cracks, their orientation, their distribution about the volume, and whether or not any anisotropy is present, as may also be expected from a compression test conducted in a uniaxial mode [34]. Although an individual object analysis can be performed within CTan, such that each individual crack becomes an object of interest, the focus here is on only the distribution of cracks about the VOI and the presence of any

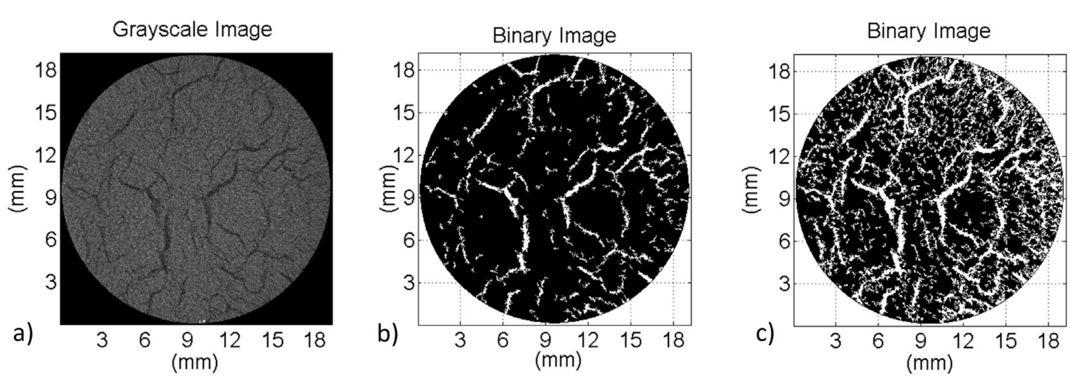


**Fig. 3.** Conversion of grayscale image generated by micro-CT reconstruction (a) to an optimal binary image (b) and an example of a much less optimal binary image (c). Specimen was strained to 5% at a constant strain rate of $1 \times 10^{-3}$ $s^{-1}$ at $-10$ °C. View is looking down the loading axis ($x_3$).

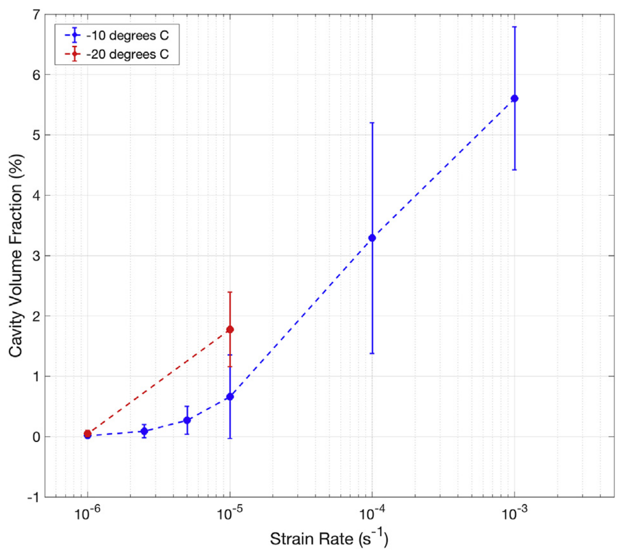


**Fig. 4.** Mean volume fraction of air to ice, calculated from 3-D binary reconstructions over all strain rates and temperatures. The mean cavity volume fraction could be considered as a metric for the volumetric crack density. Error bars represent one standard deviation from the mean with n = 4 samples.

anisotropy within this distribution of crack orientations. To further elucidate this point, Fig. 5 shows images for tests conducted at $1 \times 10^{-4}$ s$^{-1}$ and $1 \times 10^{-5}$ s$^{-1}$ at temperatures of $-10$ °C and $-20$ °C, respectively, when viewed along the loading direction $x_3$ (top view) vs. perpendicular to the loading direction $x_1$ or $x_2$ (side view). In these images, a clear example of anisotropy exists in the crack orientation, such that most cracks formed parallel to the loading direction. This trend was apparent throughout all specimens analyzed with the micro-CT, except at the lower strain rates ($\leq 5 \times 10^{-6}$ s$^{-1}$), where virtually no cracking and only plastic deformation was observed. Previously, such information about the 3-D anisotropy of damage within a specimen would have been difficult to ascertain, normally extrapolated from a 2-D analysis, but with micro-CT imagery and reconstruction such characteristics become readily apparent. To account for this anisotropy in calculations, the implementation of a crack density tensor and not just a scalar variable, remains necessary. Additional micro-CT images and views, as well as micro-CT animations, are provided in the supplementary material.

Supplementary video related to this article can be found at http://dx.doi.org/10.1016/j.actamat.2017.01.046.

### 4.2. Extension of the crack density tensor

In order to account for all x, y, and z components of the crack orientation distribution and resultant anisotropy, a variant of $\alpha_{3-D}$ (Eq. (2)) is proposed here, which to the author's knowledge has never before been proposed or applied to ice. Key to this variant of $\alpha_{3-D}$, is the 3-D stereological analysis introduced in Section 2.2 and the concept of a mean intercept length. It could perhaps also be interpreted as an inverse crack density tensor, but it will be shown in this section that the materials anisotropy tensor is of equal measure.

Given that all crack lengths and orientations within a particular VOI can be reasonably and statistically represented as an ellipsoid, Eq. (2) can be modified such that $a_i$ becomes$l_i$ and $\vec{n}\,\vec{n}$ becomes $\vec{e}_i\,\vec{e}_i$, where $l_i$ is the mean intercept length in each of the three orthogonal directions of the ellipsoid, represented by the three eigenvectors $\vec{e}_i$. Making this substitution yields a volume-averaged and inverse variant of the crack density tensor $\langle \alpha_{3-D} \rangle_V$, where Eq. (2) becomes that given in Eq. (4).

$$\langle \alpha_{3-D} \rangle_V = \frac{1}{V}\left( l_1^3 \vec{e}_1 \vec{e}_1 + l_2^3 \vec{e}_2 \vec{e}_2 + l_3^3 \vec{e}_3 \vec{e}_3 \right) \tag{4}$$

In this equation, the importance of crack orientation and length is conserved, but it should be noted that $\vec{e}_i$ is in the same orientation as that in which the mean linear intercept length $l_i$ was measured. Again, if a scalar representation of crack density is desired, then $\langle tr\alpha_{3-D} \rangle_V$ yields such a result, as the first invariant of $\langle \alpha_{3-D} \rangle_V$. To show the effectiveness of $\alpha_{3-D\ V}$ in demonstrating the anisotropy in damage observed over all compression tests, the ratios $\langle \alpha_{3-D} \rangle_{V_{22}} / \langle \alpha_{3-D} \rangle_{V_{11}}$, $\langle \alpha_{3-D} \rangle_{V_{33}} / \langle \alpha_{3-D} \rangle_{V_{11}}$, and $\langle \alpha_{3-D} \rangle_{V_{33}} / \langle \alpha_{3-D} \rangle_{V_{22}}$ are shown in Fig. 6a as functions of the applied strain rate at $-10$ °C. For comparison to the material anisotropy tensor $M$ (see Section 2.2), the ratios $M_{22}/M_{11}$, $M_{33}/M_{11}$, and $M_{33}/M_{22}$ are also shown in Fig. 6b. In these figures, it can be seen that very little anisotropy exists between $l_1$ and $l_2$ and their respective orientations $\vec{e}_1$ and $\vec{e}_2$. However, between $l_1$ and $l_3$ and $l_2$ and $l_3$, an anisotropy exists, as for a perfectly isotropic medium all ratios would have been equal to 1. Also, and perhaps not surprisingly, the trends observed in Fig. 6a and b are quite similar, as they are both based on the mean intercept length and orientation, which suggests that $M$ is a direct measurement of anisotropy in the crack orientation as well, without the need of calculating $\langle \alpha_{3-D} \rangle_V$. If allowing for this substitution, Eq. (4) then gives

$$\langle \alpha_{3-D} \rangle_M = \frac{1}{V}\left( l_1^3 M + l_2^3 M + l_3^3 M \right)$$

which simplifies to

$$\langle \alpha_{3-D} \rangle_M = \frac{M}{V}\left( l_1^3 + l_2^3 + l_3^3 \right) \tag{5}$$

where $\langle \alpha_{3-D} \rangle_M$ remains a unitless second-rank tensor representation of the crack orientation and mean intercept length. For comparison in tensor form, one example of $\langle \alpha_{3-D} \rangle_V$ and $\langle \alpha_{3-D} \rangle_M$ from a single compression test at each strain rate and at $-10$ °C is given in Table 1.

### 4.3. Crack density distribution

While both the traditional crack density tensor and the newly proposed variant of the crack density tensor give information about the anisotropy of crack orientation, they equally lack information about the three-dimensional distribution of cracks about the entire VOI. For this, a simple eigenanalysis is more useful. In addition to obtaining eigenvectors with CTan, eigenvalues ($E_1$, $E_2$, $E_3$) are also computed. These eigenvalues correlate directly to the coefficients of the ellipsoid given in Eq. (3). Because the eigenvalues represent the geometric transformation of the axes of the ellipsoid ($\vec{e}_1$, $\vec{e}_2$, $\vec{e}_3$) back to the principal axes of the scanned volume ($x_1$, $x_2$, $x_3$) of unit length, a larger eigenvalue corresponds to a greater degree of "stretching" or "compressing" of that axis. Thus, large eigenvalues correspond to large geometric transformations of that axis. Fig. 7a shows the mean eigenvalues ($\overline{E_1}$, $\overline{E_2}$, $\overline{E_3}$) calculated for each constant strain rate test at $-10$ °C. In this figure, the similarities in $\overline{E_1}$ and $\overline{E_2}$ demonstrate the relative isotropy observed with respect to the $x_1$ and $x_2$ axes. At the same time, decreasing values of $\overline{E_3}$ with increasing strain rate demonstrates an increasing number of intercepts in $x_3$. This occurs because at low strain rates, cracking

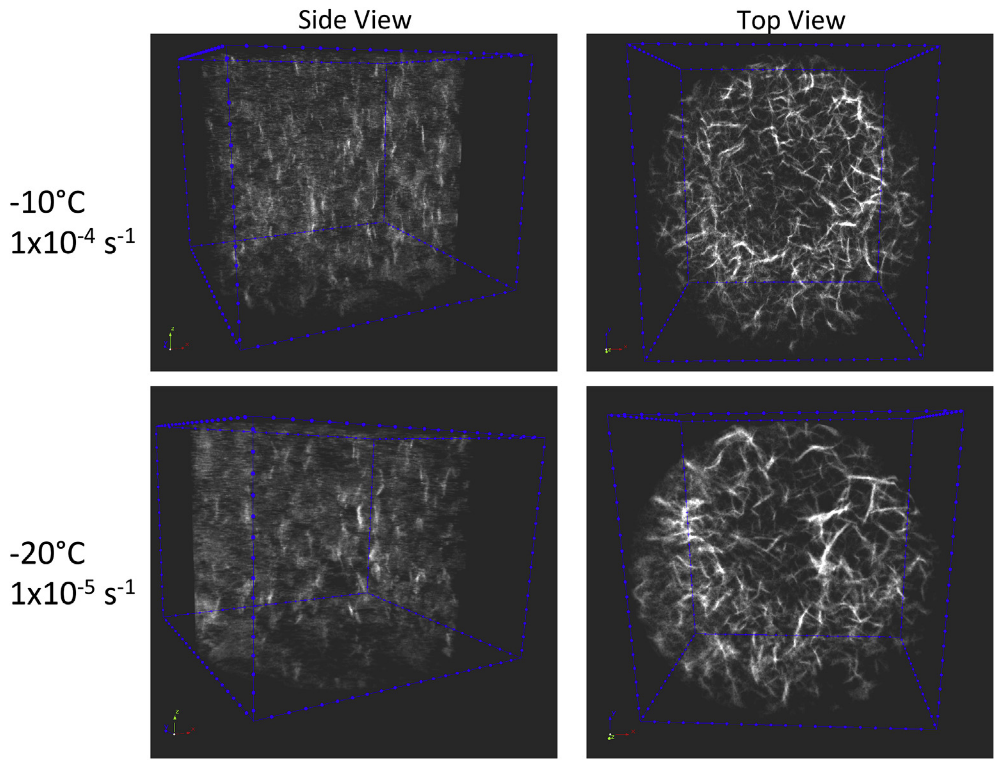


**Fig. 5.** Micro-CT reconstructions of binary images taken from specimens tested at constant strain rates of $1 \times 10^{-4}$ s$^{-1}$ at $-10$ °C (upper) and $1 \times 10^{-3}$ s$^{-1}$ at $-20$ °C (lower). This view was generated with micro-CT software that maximally limits attenuation, giving a transparent appearance. Distance between blue dots encompassing each image denote a 1 mm scale. Top view is looking down the loading direction ($x_3$). (For interpretation of the references to colour in this figure legend, the reader is referred to the web version of this article.)

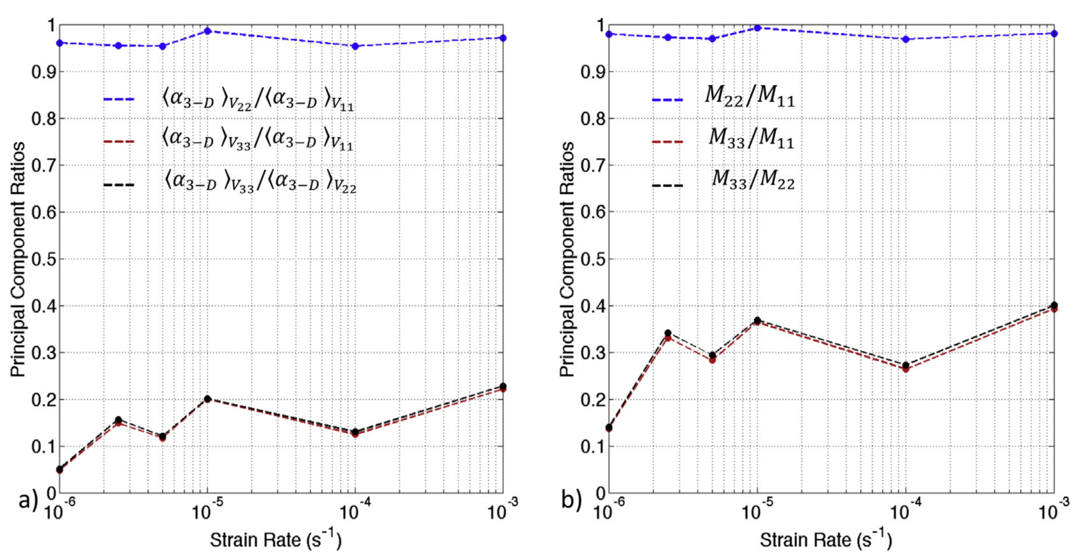


**Fig. 6.** Principal component ratios from (a) the proposed volumetric crack density tensor $\langle\alpha_{3-D}\rangle_V$ (see Eq. (4)) and (b) the materials anisotropy tensor $M$ (see Section 2.2) at $-10$ °C.

begins in only select regions and is not uniform over the entire sample volume. This creates an anisotropy in the crack orientation and relative distribution about the VOI, as evidenced by taking the trace of Eq. (5), $tr\alpha_{3-D\ M}$, as shown in Fig. 7b. Here, the decreasing trend of $\langle tr\alpha_{3-D}\rangle_M$ with increasing strain rate provides evidence of the crack distribution becoming more uniform as more cracks begin filling out the VOI.

## 5. Discussion

The results presented in Section 4 of this study are thought to be of significance, as similar previous laboratory studies on the mechanical properties of polycrystalline ice [8,14,16] have not yet been able to quantify, in situ or in three dimensions, many of the important characteristics of the damage which they had observed. For example, quantifying the crack shape, crack connectivity, 3-D

**Table 1**
Variants of the crack density tensor calculated with Eqs. (4) and (5) from one test at each constant applied strain rate at −10 °C.

| Strain rate | $\langle\alpha_{3-D}\rangle_V = \frac{1}{V}(l_1^3\vec{e}_1\vec{e}_1 + l_2^3\vec{e}_2\vec{e}_2 + l_3^3\vec{e}_3\vec{e}_3)$ | $\langle\alpha_{3-D}\rangle_M = \frac{M}{V}(l_1^3 + l_2^3 + l_3^3)$ |
|---|---|---|
| $1 \times 10^{-3}\ s^{-1}$ | 8.30e-07 1.79e-08 -3.79e-09 | 8.26e-05 -2.44e-06 -8.21e-07 |
| | 1.79e-08 8.09e-07 2.33e-09 | −2.44e-06 8.40e-05 1.28e-06 |
| | −3.79e-09 2.33e-09 2.64e-07 | −8.21e-07 1.28e-06 1.77e-04 |
| $1 \times 10^{-4}\ s^{-1}$ | 1.23e-06 -2.74e-08 3.61e-09 | 8.76e-05 2.72e-06 -8.68e-07 |
| | −2.74e-08 1.16e-06 2.20e-09 | 2.72e-06 9.10e-05 -1.32e-06 |
| | 3.61e-09 2.20e-09 2.28e-07 | −8.68e-07 -1.32e-06 2.69e-04 |
| $1 \times 10^{-5}\ s^{-1}$ | 4.38e-07 -1.11e-08 -5.34e-10 | 6.47e-05 2.09e-06 -1.96e-07 |
| | −1.11e-08 4.62e-07 2.67e-10 | 2.09e-06 6.24e-05 4.31e-07 |
| | −5.34e-10 2.67e-10 7.32e-08 | −1.96e-07 4.31e-07 2.13e-04 |
| $5 \times 10^{-6}\ s^{-1}$ | 4.85e-06 -3.18e-07 7.58e-09 | 1.41e-04 1.28e-05 -1.88e-06 |
| | −3.18e-07 4.64e-06 1.29e-08 | 1.28e-05 1.45e-04 -1.13e-06 |
| | 7.58e-09 1.29e-08 1.01e-06 | −1.88e-06 -1.13e-06 3.98e-04 |
| $2.5 \times 10^{-6}\ s^{-1}$ | 1.76e-07 -4.15e-08 2.73e-10 | 4.68e-05 1.50e-05 -2.27e-07 |
| | −4.15e-08 1.73e-07 6.06e-11 | 1.50e-05 4.72e-05 -5.37e-07 |
| | 2.73e-10 6.06e-11 2.16e-08 | −2.27e-07 -5.37e-07 1.83e-04 |
| $1 \times 10^{-6}\ s^{-1}$ | 1.72e-07 9.85e-09 8.58e-10 | 4.64e-05 -3.25e-06 -1.20e-06 |
| | 9.85e-09 1.90e-07 5.10e-10 | −3.25e-06 4.35e-05 -2.36e-06 |
| | 8.58e-10 5.10e-10 1.20e-08 | −1.20e-06 -2.36e-06 2.74e-04 |

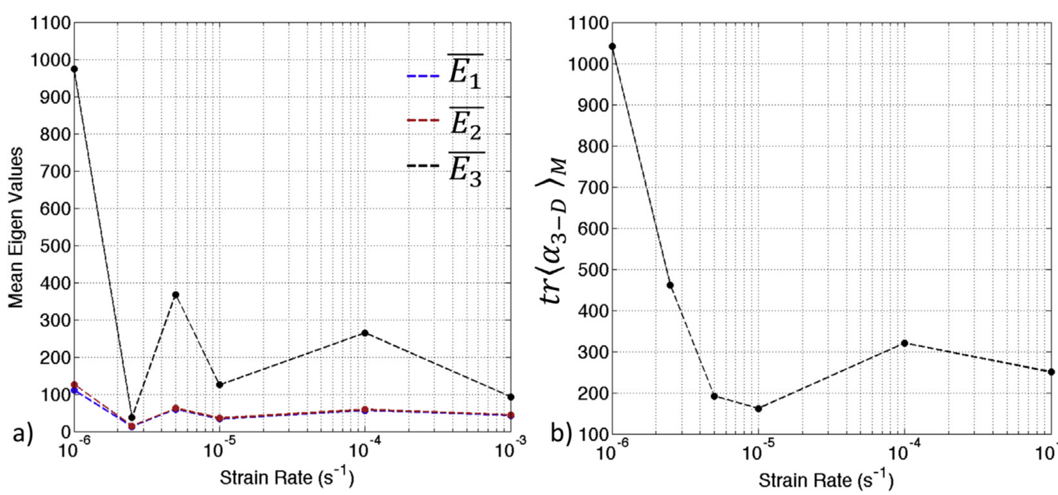


**Fig. 7.** Mean eigenvalues for all constant strain rate tests at −10 °C (a) and $tr\langle\alpha_{3-D}\rangle_M$ for all constant strain rate tests (b).

crack orientation, and/or spatial distribution of cracks could allow for a more rigorous 3-D model to be developed relating the elasticity and porosity of ice [8,33]. Although this end was beyond the scope of the work presented here, it has now been shown to be well within the realm of what is possible with micro-CT. Additionally, as shown in Fig. 4 for the data collected at −10 °C, it is possible that an exponential relationship may exist between the rate of cavity growth and the imposed strain rate in polycrystalline ice. If these experiments were to be repeated as a function of strain instead of strain rate, for instance, it is thought to be possible with the micro-CT approach presented here that such information could lend additional insight into the mechanics of cavity/crack development in ice and whether there is a strain dependency indicative of a more ductile or brittle regime of deformation occurring locally [40]. With the introduction of the quantitative techniques presented in this study, combined with the many other recent advances in the quantification of damage and deformation in other polycrystalline materials via micro-CT [41], it is proposed here that a new paradigm in the laboratory study of polycrystalline ice is possible.

## 6. Conclusions

It has been shown that the use of X-ray computed microtomography can be extended to the study of damage and the onset of micro-cracking in polycrystalline ice. This was demonstrated through the detailed analysis of a set of experiments where laboratory-prepared samples of polycrystalline ice, of a 1 mm mean grain diameter, were strained at six strain rates spanning four orders of magnitude and two different test temperatures. It was found that a clear anisotropy exists in both the orientation and distribution of micro-cracks and that these features could be quantified and measured via existing an/sid commercially available software for micro-CT. Additionally, it was found that two individual measurements of anisotropy are necessary for measuring the anisotropy of crack orientation vs. crack distribution, and that these can both be determined with a mean intercept length analysis and quantified with the materials anisotropy tensor, as first given in Harrigan & Mann (1984) [35]. Using this approach, a new and alternative form of the traditional crack density tensor was introduced. In future work, the mechanisms responsible for the damage observed in these test specimens, as well as their connectivity as a function of strain, will be addressed.


## Acknowledgements

This work was supported by NSF grant # 1141411. The authors thank Professor Carl Renshaw for his helpful comments and acknowledge the use of the Dartmouth Ice Research Laboratory for

this work (Director E.M. Schulson).

## References


[1] S.R. Stock, Microcomputed Tomography: Methodology and Applications, CRC Press, Boca Raton, FL, 2009.
[2] E.N. Landis, D.T. Keane, X-ray microtomography, Mater. Charact. 61 (2010) 1305–1316.
[3] M.L. Bouxsein, S.K. Boyd, B.A. Christiansen, R.E. Guldberg, K.J. Jepsen, R. Müller, Guidelines for assessment of bone microstructure in rodents using micro-computed tomography, J. Bone Min. Res. 25 (7) (2010) 1468–1486.
[4] R.W. Obbard, G. Troderman, I. Baker, Imaging brine and air inclusions in sea ice using micro-X-ray computed tomography, J. Glaciol. 55 (2009) 1113–1115.
[5] E.N. Landis, Damage variables based on three-dimensional measurements of crack geometry, Strength, Fract. Complex. 3 (2–4) (2005) 163–173.
[6] M. Schneebeli, S.A. Sokrato, Tomography of temperature gradient metamorphism of snow and associated changes in heat conductivity, Hydrol. Process. 18 (18) (2005) 3655–3665.
[7] J. Réthoré, N. Limodin, J.Y. Buffière, S. Roux, F. Hild, Three-dimensional analysis of fatigue crack propagation using X-Ray tomography digital volume correlation and extended finite element simulations, Procedia IUTAM 4 (2012) 151–158.
[8] S.A. Snyder, E.M. Schulson, C.E. Renshaw, The role of damage and recrystallization in the elastic properties of columnar ice, J. Glaciol. 61 (227) (2015) 461–480.
[9] L.W. Gold, The Failure Process in Columnar-grained Ice. Tech. Paper No. 369 of the Division of Building Research, National Research Council of Canada, Ottawa, 1972.
[10] I. Hawkes, M. Mellor, Deformation and fracture of ice under uniaxial stress, J. Glaciol. 11 (1972) 103–131.
[11] E.M. Schulson, The brittle compressive fracture of ice, Acta Metall. Mater 38 (1990) 1963–1976.
[12] M.A. Rist, S.A.F. Murrell, Ice triaxial deformation and fracture, J. Glaciol. 40 (1994) 305–318.
[13] M. Arakawa, N. Maeno, Mechanical strength of polycrystalline ice under uniaxial compression, Cold Reg. Sci. Technol. 26 (1997) 215–229.
[14] D. Iliescu, E.M. Schulson, Brittle compressive failure of ice: monotonic versus cyclic loading, Acta Mater 50 (2002) 2163–2172.
[15] E.M. Schulson, P. Duval, Creep and Fracture of Ice, Cambridge University Press, 2009.
[16] S.A. Snyder, E.M. Schulson, C.E. Renshaw, Effects of prestrain on the ductile-to-brittle transition of ice, Acta Mater 108 (2016) 110–127.
[17] D.G. Vaughan, C.S.M. Doake, Recent atmospheric warming and retreat of ice shelves on the Antarctic Peninsula, Nature 379 (1996) 328–331.
[18] M.A. Rist, P. Sammonds, H. Oerter, C.S.M. Doake, Fracture of Antarctic shelf ice, J. Geophys. Res. Solid Earth 107 (B1) (2002).
[19] N. Urabe, T. Iwasaki, A. Yoshitake, Fracture toughness of sea ice, Cold Reg. Sci. Technol. 3 (1980) 29–37.
[20] G.A. Kuehn, E.M. Schulson, The mechanical properties of saline ice under uniaxial compression, Ann. Glaciol. 19 (1994) 39–48.
[21] E.T. Gratz, E.M. Schulson, Brittle failure of columnar saline ice under triaxial compression, J. Geophys. Res. 102 (1997) 5091–5107.
[22] E.M. Schulson, A. Fortt, D. Iliescu, C.E. Renshaw, Failure envelope of first-year Arctic sea ice: the role of friction in compressive fracture, J. Geophys. Res. 111 (2006) C11S25.
[23] J. Schwarz, W.F. Weeks, Engineering properties of sea ice, J. Glaciol. 19 (1977) 499–531.
[24] P.R. Sammonds, S.A.F. Murrell, M.A. Rist, Fracture of multi-year sea ice, J. Geophys. Res. 103 (C10) (1998) 21795–21815.
[25] E.M. Schulson, Brittle failure of ice, Eng. Fract. Mech. 68 (2001) 1839–1887.
[26] R. Greenberg, P. Geissler, G. Hoppa, B.R. Tufts, D.D. Durda, R. Pappalardo, J.W. Head, R. Greeley, R. Sullivan, M.H. Carr, Tectonic processes on Europa: tidal stresses, mechanical response, and visible features, Icarus 135 (1998) 64–78.
[27] E.M. Schulson, On the origin of a wedge crack within the icy crust of Europa, J. Geophys. Res. 107 (E11) (2002) 5701.
[28] M.L. Rudolph, M. Manga, Fracture penetration in planetary ice shells, Icarus 199 (2009) 536–541.
[29] L.W. Gold, Statistical characteristics for the type and length of deformation-induced cracks in columnar-grain ice, J. Glaciol. 43 (1997) 311–320.
[30] X. Wang, I. Baker, Evolution of the specific surface area of snow during high temperature gradient metamorphism, J. Geophys. Res.-Atmos. 119 (24) (2014) 13690–13703.
[31] K. Hammonds, R. Lieb-Lappen, I. Baker, X. Wang, Investigating the thermophysical properties of the ice-snow interface under a controlled temperature gradient – Part I: experiments and Observations, Cold Reg. Sci. Technol. 120 (2015) 157–167.
[32] M.L. Kachanov, Continuum model of medium with cracks, J. Eng. Mech. Div. 106 (5) (1980) 1039–1051.
[33] M.L. Kachanov, Effective elastic properties of cracked solids: critical review of some basic concepts, Appl. Mech. Rev. 45 (8) (1992) 304–335.
[34] V.A. Lubarda, D. Krajcinovic, Damage tensors and the crack density distribution, Int. J. Solids Struct. 30 (20) (1993) 2859–2877.
[35] T.P. Harrigan, R.W. Mann, Characterization of microstructural anisotropy in orthotropic materials using a second rank tensor, J. Mat. Sci. 19 (1984) 761–767.
[36] D.M. Cole, Preparation of polycrystalline ice specimens for laboratory experiments, Cold Reg. Sci. Technol. 1 (1979) 153–159.
[37] ASTM E1382-97, Standard Test Methods for Determining Average Grain Size Using Semiautomatic and Automatic Image Analysis, ASTM International, West Conshohocken, PA, 2004.
[38] K. Hammonds, I. Baker, The effects of $Ca^{++}$ on the strength of polycrystalline ice, J. Glaciol. 62 (235) (2016) 954–962.
[39] L.M. Kachanov, Rupture time under creep conditions, Int. J. Frac. 97 (1–4) (1999) 11–18.
[40] A.C.F. Cocks, M.F. Ashby, Intergranular fracture in power law creep under multiaxial stress, Metal Sci. 14 (1980) 395–402.
[41] E. Maire, P.J. Withers, Quantitative X-ray tomography, Int. Mater. Rev. 59 (1) (2014) 1–43.